Journal of Molecular Structure 1353 (2026) 144582

Contents lists available at ScienceDirect

Journal of Molecular Structure

journal homepage: www.elsevier.com/locate/molstr

Influence of mono- and di-bromo substitution on the structure conformation and supramolecular assembly of schiff base derivatives

Udaya Kumar A. H. [a], Yuvaraja Dibdalli [b], Cesar Morales-Verdejo [c], Nagesh Khadri M. J. [d], Mahesha [b,e,*], Lokanath N. K. [f,*]

[a] Department of Physics, Seshadripuram Institute of Technology, Kadakola, Mysuru 571311, Karnataka, India
[b] Centro Integrativo de Biología y Química Aplicada (CIBQA), Facultad de Ciencias de la Salud, Universidad Bernardo O'Higgins, General Gana, Santiago 1702, Chile
[c] Universidad Bernardo OHiggins, Vicerrectoría Académica, Dirección General de Investigación, Innovación, Transferencia y Emprendimiento, General Gana 1702, Santiago, Chile
[d] Department of Chemistry, Seshadripuram Institute of Technology, Kadakola, Mysuru 571311, Karnataka, India
[e] Department of Physics, SJCE, JSS Science and Technology University, Mysuru 570 006, Karnataka, India
[f] Department of Studies in Physics, University of Mysore, Manasagangotri, Mysuru, 570 006, Karnataka, India

ARTICLE INFO

Keywords:
Schiff base
π···π stacking interactions
QTAIM
Antibacterial studies
Molecular docking

ABSTRACT

The positioning of substituents plays a critical role in dictating molecular conformation and supramolecular assembly, essential for the rational design of functional crystalline materials. In this work, two Schiff base compounds were synthesized via the condensation of ethyl 2-aminoisonicotinate with 3-bromo-5-hydroxybenzaldehyde and 3,5-dibromo-5-hydroxybenzaldehyde. Single crystals suitable for X-ray diffraction were obtained by slow evaporation, and both compounds crystallized in the triclinic space group $P\bar{1}$. Structural analysis revealed nearly planar geometries with dihedral angles between the hydroxyphenyl and ethoxypyridyl moieties, connected through an azomethine bridge. The planarity facilitated robust π–π stacking interactions and hydrogen bonding, both contributing to crystal packing stabilization. Comparative assessment showed that the second bromine atom significantly modifies intermolecular interactions and supramolecular organization. Hirshfeld surface, fingerprint plots, enrichment ratios, and QTAIM analyses quantitatively characterized these contacts, while DFT calculations indicated enhanced π-electron delocalization and reduced HOMO–LUMO gaps. Molecular docking against *Staphylococcus aureus* TyrRS revealed π-stacking-mediated ligand–receptor interactions with good binding energies, highlighting biological relevance. This study provides quantitative insight into how positional substitution governs molecular packing, noncovalent interactions, and protein-ligand interaction leading to the potential functional applications.

1. Introduction

Crystal engineering—the design and synthesis of molecular solids with targeted structural and functional properties—relies fundamentally on the control of intermolecular interactions within the solid state [1–3]. Among these, noncovalent forces such as hydrogen bonding, π–π stacking, halogen bonding, and dipolar interactions serve as key drivers of molecular recognition and crystal packing. In aromatic systems, the nature, number, and position of substituent groups significantly affect both molecular conformation and the resulting supramolecular architectures [4–8].

Substituent effects on crystal structure can be rationalized in terms of electronic influences (e.g., inductive and resonance contributions) and steric parameters [9–11]. These effects manifest in the modulation of key packing motifs such as π–π interactions, hydrogen-bond networks, and directional halogen contacts. Notably, substituent positioning whether at the ortho, meta, or para sites of an aromatic ring can drastically alter molecular planarity, and the resulting supramolecular architectures, and ultimately, material properties. For instance, ortho-substitution often induces steric hindrance, leading to nonplanar conformations and disrupted π-stacking, whereas para-substitution typically supports planar backbones and promotes columnar or layered assemblies [12–16].

Recent studies have demonstrated the significance of such

* Corresponding authors.
E-mail addresses: arjunrmahi@gmail.com (Mahesha), lokanath@physics.uni-mysore.ac.in (L. N. K.).

https://doi.org/10.1016/j.molstruc.2025.144582
Received 9 August 2025; Received in revised form 20 October 2025; Accepted 29 October 2025
Available online 30 October 2025

substituent effects in functional materials. Methoxy-substituted small molecules have shown substantial changes in optoelectronic properties and π–π stacking behavior based solely on positional variation [17–19]. Likewise, halogen substituents have proven to be critical in controlling supramolecular diversity through specific C–H···X and halogen···π interactions. However, while mono-substituent effects have been extensively explored, the influence of secondary substitution, particularly at varying positions relative to a primary group, remains poorly understood. In supramolecular chemistry, the design and synthesis of di-substituted aromatic systems offer expanded opportunities for engineering intermolecular contacts, including cooperative or competitive interaction pathways. These effects are primarily attributed to electronic influences, such as inductive and resonance contributions, and steric parameters. However, while mono-substituent effects have been extensively explored, the influence of secondary substitution, particularly at varying positions relative to a primary group, remains poorly understood. This gap in knowledge underscores the need for systematic studies that investigate the interplay between substituent positioning and molecular packing, noncovalent interactions, and functional applications. Such studies are crucial for the rational design of functional crystalline materials with tailored properties.

Despite the growing understanding of mono-substituent effects on molecular conformation and crystal packing, the systematic study of dual substitution patterns remains limited. Investigating how the position and nature of multiple substituents influence supramolecular assembly is critical for designing functional crystalline materials with predictable properties. Moreover, integrating experimental crystallography with computational analyses, such as density functional theory (DFT), Hirshfeld surface mapping, and molecular docking, allows for a deeper understanding of electronic structure, intermolecular interactions, and potential biological relevance. In this context, our study focuses on Schiff base compounds with mono- and di-bromo substitutions, aiming to elucidate the interplay between substituent positioning, noncovalent interactions, and crystal packing, as well as to explore their interaction with protein targets. This combined approach provides both structural insights and functional implications, thereby addressing gaps in the existing literature and offering a rational framework for the design of advanced materials and bioactive molecules.

2. Materials and methods

2.1. Synthesis of (E)-ethyl 2-((3,5-dibromo-2-hydroxybenzylidene) amino)isonicotinate

All chemicals and solvents employed in this research work were procured from Sigma-Aldrich, India, and were utilized without additional purification. In a round-bottom flask, 1 mmol of ethyl 2-aminoisonicotinate was dissolved in 10 ml of ethanol. Simultaneously, 1 mmol of 3,5-dibromohydroxy-benzaldehyde was dissolved in 10 ml of ethanol in another beaker. The aldehyde solution was then slowly added drop by drop to the ethanolic amine solution while maintaining stirring at 60 °C. Initially, the solution colour turned pale red, indicating the reaction initiation, and refluxing was sustained. After 3 h of refluxing, a red precipitate formed and the schematic representation is shown in Scheme 1. The product was subsequently collected, dried. The product was obtained in 68 % yield. The obtained compound was subjected to slow evaporation in methanol. Following a period of 20 days, red crystals of the Schiff base derivatives were obtained. The melting points of compounds 1 and 2 were determined to be 173.04 °C and 165.0 °C, respectively. The formation of the compounds was initially confirmed by spectroscopic analyses, including FTIR spectroscopy (Fig. S1). The ^{1}H and ^{13}C NMR spectra of compound 1 (Figs. S2 and S3) and compound 2 (Figs. S4 and S5) are presented in the Supporting Information. Furthermore, the mass spectra of compounds 1 and 2 are provided in Figs. S6 and S7, respectively.

2.2. Single crystal X-ray diffraction studies

Good-quality single crystals were assessed using the polarizing microscope and selected for the experimental analysis. Rigaku Xtalab mini single crystal X-ray diffractometer equipped with graphite monochromator and Mo Kα (λ=0.71073 Å) radiation was used for X-ray intensity data collection. The crystal quality was assessed by analyzing the initial twelve frames and further, it was utilized for data collection strategy calculations. The collected intensity data were corrected for Lorentz, polarization and absorption effects using the *d*trek* program [20]. The molecular structure was solved by the intrinsic phasing method using SHELXT [21]and the structure refinement was performed using SHELXL by utilizing the full matrix least-squares on the F^2 method [22]. The non-hydrogen atoms are identified by the Fourier map and refined anisotropically, while hydrogen atoms are located in the calculated positions and refined isotropically by the riding model. The crystal data and refinement parameters of the compound are tabulated in Table 1. The molecular geometry, noncovalent interactions and crystal packing topology are obtained using *Platon* and *Mercury* software [23, 24]. The comparison of the geometrical parameters is listed in Table S1-S6.

2.3. Noncovalent interactions analysis

2.3.1. Hirshfeld surface analysis

For visualization of the 3-D spatial arrangement and relevance of interatomic contacts by unique colour code, molecular Hirshfeld surface (HS) and 2-D fingerprint plots were carried out using *Crystal Explorer* software [25].

The HS is mapped over $d_{norm,}$ which is based on d_i, d_e (distance between HS and the nearest atom internal/external) and their van der Walls radii. Employing the above data, it identifies various atomic contacts and provides the strength of each via graphical representation [26,27]. Further, the shape index is a surface property to measure the shape and it is very sensitive to subtle changes in surface shape. One important attribute of the shape index is that two shapes where the shape index differs only by a sign represent complementary "stamp" and "mould" pairs. The shape index depicted on the Hirshfeld surface (HS). It

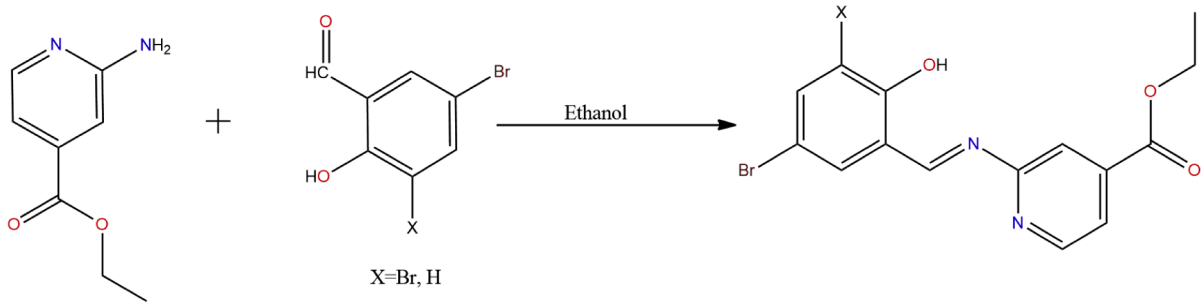

Scheme 1. Synthesis outline of Schiff base mono- and di-bromo Schiff base derivatives.

Table 1
Crystal structure data and refinement parameters of the compounds.

	Compound 1 (SV3)	Compound 2 (SV2)
CCDC No.	2478,800	2351,696
Empirical formula	$C_{15}H_{13}Br_1N_2O_3$	$C_{15}H_{12}Br_2N_2O_3$
Formula weight	349.18	428.09
Temperature/K	193	293.15
Crystal system	Triclinic	Triclinic
Space group	$P\bar{1}$	$P\bar{1}$
a/Å	7.591(3)	7.989(2)
b/Å	9.376(4)	9.060(3)
c/Å	10.891(5)	11.101(3)
α/°	106.454(8)	101.119(7)
β/°	99.123(8)	93.645(7)
γ/°	100.338(8)	99.753(7)
Volume/Å^3	713.1(5)	773.2(4)
Z	2	2
ρ_{calc} g/cm^3	1.626	1.839
μ/mm^{-1}	2.894	5.256
F_{000}	352.0	420.0
Crystal size/mm^3	0.21 × 0.27 × 0.34	0.23 × 0.32 × 0.27
Radiation	MoKα (λ = 0.71073)	MoKα (λ = 0.71073)
2θ range for data collection/°	6.114 to 54.936	6.106 to 54.968
Index ranges	$-9 \le h \le 7$, $-12 \le k \le 10$, $-13 \le l \le 14$	$-10 \le h \le 10$, $-7 \le k \le 11$, $-13 \le l \le 14$
Reflections collected	4107	4603
Independent reflections	3158 [R_{int} = 0.0582, R_{sigma} = 0.1511]	3470 [R_{int} = 0.0538, R_{sigma} = 0.1150]
Data/restraints/parameters	3158/0/192	3470/0/201
Goodness-of-fit on F^2	1.019	0.993
Final R indexes [I>=2σ(I)]	R_1 = 0.0809, wR_2 = 0.1518	R_1 = 0.0738, wR_2 = 0.1601
Final R indexes [all data]	R_1 = 0.1769, wR_2 = 0.1830	R_1 = 0.1108, wR_2 = 0.1828
Largest diff. peak/hole / e Å^{-3}	0.49/−0.65	1.01/−1.63

can be employed to discern C—H···π and π···π interactions by observing corresponding hollows and bumps as well as adjacent red and blue triangles, respectively.

2.3.2. Fingerprint and enrichment ratio analyses

A fingerprint (FP) plot of intermolecular interactions provides information regarding the various atomic contacts present within a molecular structure. These 2D-FP plots, derived from the HS, visually summarize the frequency of each combination of d_e and d_i across the molecular surface [28–32], Therefore, they not only reveal the presence of specific intermolecular interactions but also indicate the relative surface area corresponding to each type of interaction. These percentages of contacts in a crystal packing can be used to identify enrichment ratios (E_{XX}). It is the ratio between the proportion of actual contacts in the crystal and the theoretical proportion of random contacts, which are obtained by considering that all contact types in the crystal packing were equidistributed between all chemical types. The ER values are expected to be typically >1 for pairs of elements that readily form contacts in crystals, while pairs that tend to avoid the contacts should produce an ER value <1 [33].

2.3.3. Quantum of the theory of atoms in molecule (QTAIM) analysis

The intramolecular interactions were studied by examining the electron density topology in the interatomic regions, employing standard protocols of QTAIM and NCI techniques [34]. It is based on two scalar fields, electron density and reduced density gradient (RDG), to map the bonding properties. In addition to the electron density ρ(r), Laplacian of electron density $\nabla^2\rho(r)$, Lagrangian kinetic electron density G(r) and the potential electron density V(r) at the bond critical point (BCP) have been investigated using *Multiwfn* software to explore the of noncovalent interactions properties of the molecule [35].

2.4. Density functional theory calculations

The molecular mechanism of any molecule is very important to envisage its behaviour. *Gaussian 16* is an electronic structure modelling software and the most used quantum computational program [36]. It does electronic-structure calculations and standard quantum chemical calculations to predict the energies, molecular structure geometries, and vibrational frequencies, along with other molecular properties derived from these basic calculations. Density functional theory (DFT) with a hybrid functional B3LYP is used to study the molecular system of the title compound. The geometry optimization was done using a 6–311+G (d,p) basis set for the determination of optimized energy and other physicochemical properties (susceptibility χ, chemical hardness η, and chemical potential μ) of the compound using Koopmann's theorem . In addition, the frequency calculation was performed to make evident the correspondence of the optimized structure with the local minima. The geometrical factors such as bond lengths, bond angles, and torsional angles were also compared with the crystal structure geometry and tabulated [34]. Further NBO calculations were performed using **NBO 3.1** to analyze donor (i) and acceptor (j) to estimate the stabilization energy related to the delocalization i → j. The optimization and electronic structure calculations were performed with *Gaussian 16* using the *Gaussview 6* visualizing platform [37].

2.5. Molecular docking studies

The crystal structure is used directly for molecular docking studies to study residue interactions, including hydrogen bonds and other interactions, and binding energy scores. The original 3D structure conformation of PDB (1JIL: Crystal structure of S. aureus TyrRS) was downloaded from the Protein Data Bank [38]. The protein was preprocessed by removal of existing ligands addition of polar hydrogens, and addition of Kollman's united atomic charges using Vina [39,40]. Then, the protein and ligand were saved in a .pdbqt format file. The ligand conformation poses were generated by using orientations within the active site of 1JIL using the Lamarckian genetic algorithm. The best pose selection was done on the basis of binding affinity, and pose retrieval was done by using the non-bonding interaction visualizer in Discovery Studio [41]. The non-covalent interaction (hydrogen and π based interactions), involving amino acid residues and the centroid ring of the ligands, play a vital role in stabilizing the ligand–protein complex, enhancing binding affinity, and contributing to the overall biological activity and potential inhibitory effect of the compounds toward TyrRS.

3. Results and discussion

3.1. Crystal structure description

3.1.1. Structure conformation description

Single-crystal X-ray diffraction analysis confirmed that both mono- and di-bromo substituted Schiff base compounds crystallized in the triclinic space group $P\bar{1}$. The ORTEP diagrams for the compounds are presented in Fig. 1, with thermal ellipsoids depicted at the 50 % probability level. Both molecule consists of a phenyl and a pyridine ring, linked through an azomethine (-CH=*N*-) moiety. The monobrominated phenyl ring of compound 1 is replaced by a dibrominated analogue in compound 2, with bromine atoms occupying both meta positions. This structural modification provides an opportunity to assess the effect of bromine substitution on molecular conformation and supramolecular architecture.

Torsion angle analysis reveals that the bridging azomethine chain (C6–C7–N1–C8) adopts *a* +anti-periplanar (+ap) conformation, with torsion angles of 178.89° and 178.01° Additionally, the ester group

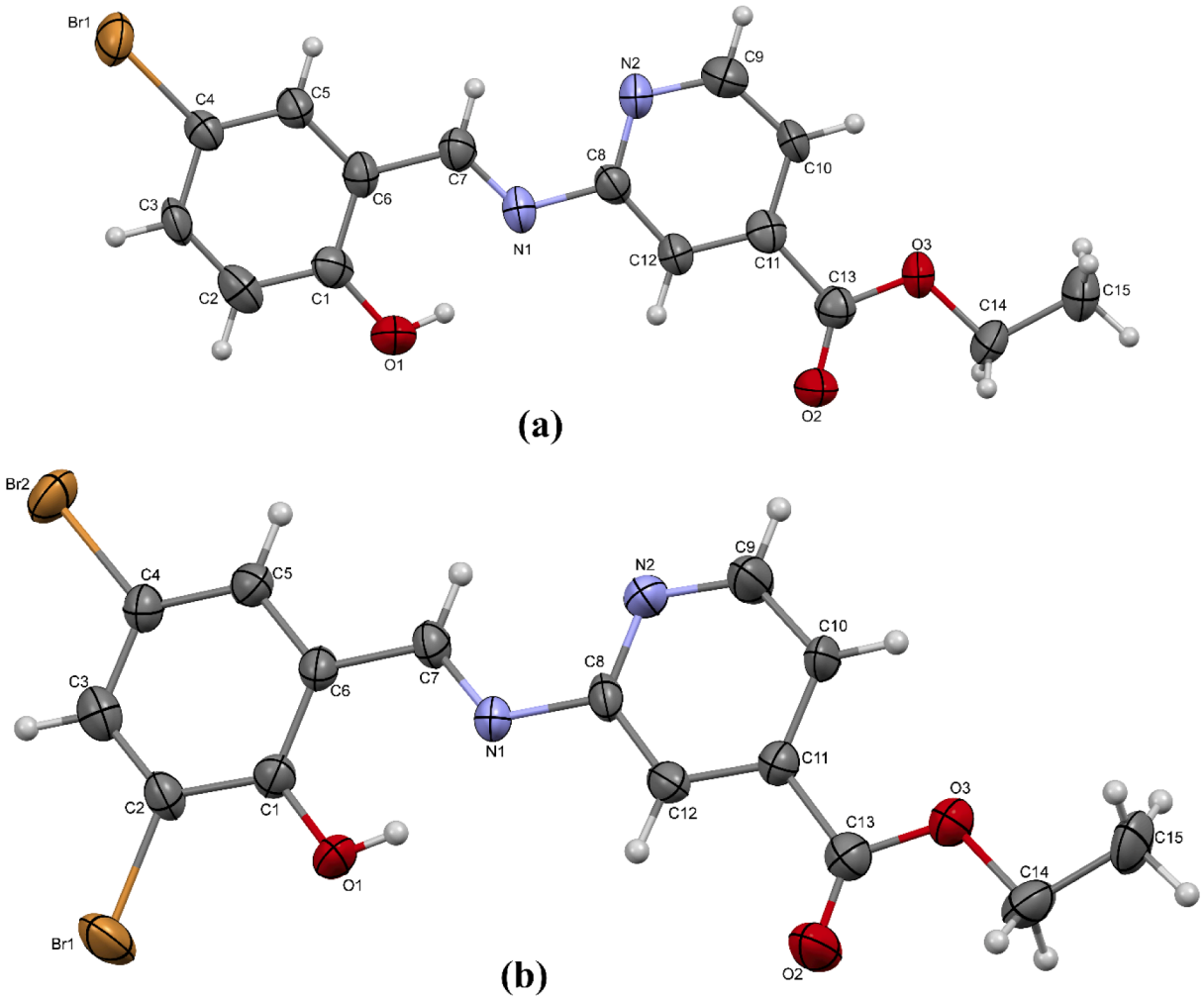

Fig. 1. ORTEP of the mono- and di-bromo substituted Schiff base derivatives.

attached to the pyridine ring exhibits a –syn-periplanar (–sp) conformation, as defined by the torsion angles C10–C11–C13–O3 = –5.09° and –1.14° respectively. The extended chain segment C13–O3–C14–C15 displays torsion angles of –167.82° and –168.29°, indicating that it remains nearly coplanar with the aromatic ring systems. The dihedral angles between the phenyl and pyridine rings are 0.95° and 3.20°, respectively, confirming the overall planarity of the molecules (Fig. S8).

3.1.2. *Supramolecular assembly description*

The molecular structures and crystal packing of both compounds are stabilized by a variety of intra- and intermolecular interactions, including O–H···N, C–H···O, C–H···N, and π···π stacking. Detailed hydrogen bond geometries are summarized in Table 2. Prominent intramolecular hydrogen bonds, namely O1–H1···N1 and C7–H7···N2, result in the formation of S(6) and S(5) pseudo-rings, respectively, as illustrated in Fig. S9. Additionally, the ester functional group contributes to three weak intramolecular hydrogen bonds (C14–H14B···O2, C12–H12···O2, and C10–H10···O3), leading to the formation of three distinct S(5) ring motifs.

In compound 1, a strong intermolecular hydrogen bond (C5–H5···O2) connects neighboring molecules into a 1-D chain along the crystallographic *b*-axis. It is further stabilized by π···π interactions between aromatic rings (C3···C11 and C1···C8), contributing to the overall packing framework (Fig. 2).

Compound 2 exhibits a notable Br···O halogen bonding interaction, forming an infinite one-dimensional chain along the *b*-axis, as depicted in Fig. 3(a). These chains are reinforced by an $R_2^1(6)$ supramolecular synthon, formed via two weak C–H···O hydrogen bonds (C5–H5···O2 and C7–H7···O2), wherein the carbonyl oxygen of the ester group acts as a bifurcated acceptor. These linear 1D motifs are interconnected via C–H···Br interactions (2.951 Å, 160.78°) to generate a 2D sheet in the *bc*-plane, as shown in Fig. 3(b). Furthermore, a C14–H14B···O1 hydrogen bond (2.705 Å, 147.27°) involving the –CH_2 group of the ester and a neighboring molecule across an inversion center contributes to the formation of a 3-D supramolecular network. In addition, π–π stacking interactions play a crucial role in the packing stability. Two distinct types of stacking interactions are observed: parallel face-to-face stacking

Table 2
Geometry details of hydrogen bonding interactions mono- and di-bromo substituted Schiff base compounds 1 and 2.

Type	D-H···A	D-H	H···A	D···A	D-H···A
Compound 1					
Intra	O1-H1···N1	0.82	1.81	2.543(7)	148
Intra	C7-H7···N2	0.93	2.39	2.725(8)	101
Inter[i]	C5-H5···O2 [i]	0.93	2.57	3.397(8)	148
Type	D-H···A	D-H	H···A	D···A	D-H···A
Compound 2					
Intra	O1-H1···N1	0.82	1.86	2.590 (8)	148
Intra	C7-H7···N2	0.93	2.38	2.729(10)	102
Inter[ii]	C5-H5···O2 [i]	0.93	2.40	3.270(9)	155

[i] . *x*, −1 + *y*, *z*.
[ii] . *x*, −1 + *y*, *z*.

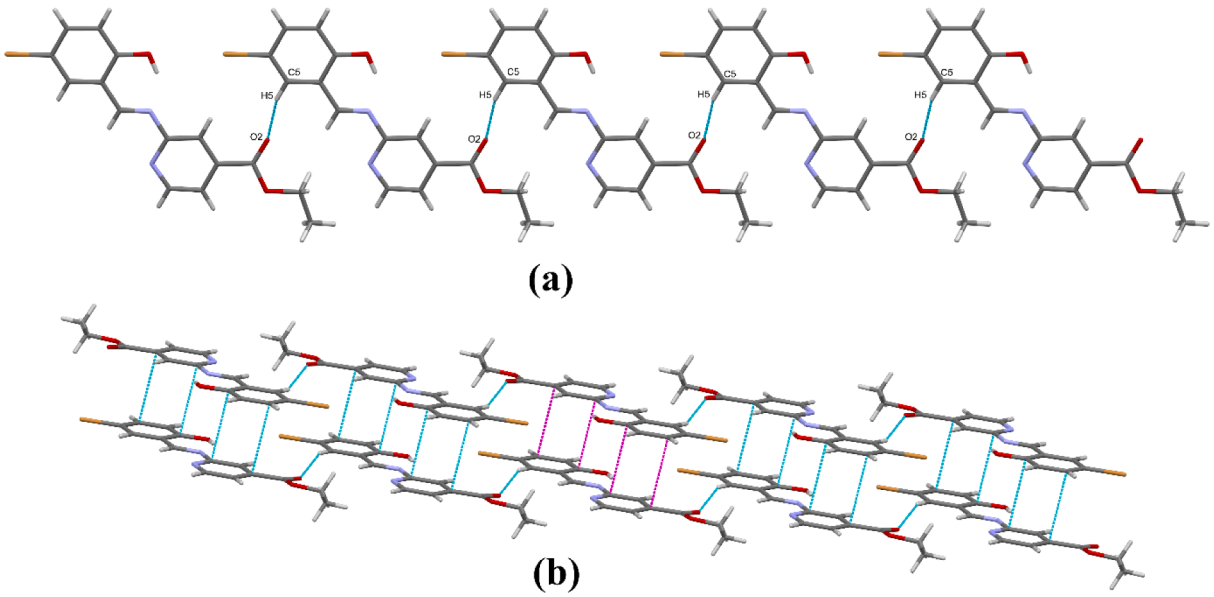

Fig. 2. (a) An infinite 1-D chain formed by C—H···O contacts (b) 2-D packing construction by π···π interactions in mono-bromo substituted Schiff base compound.

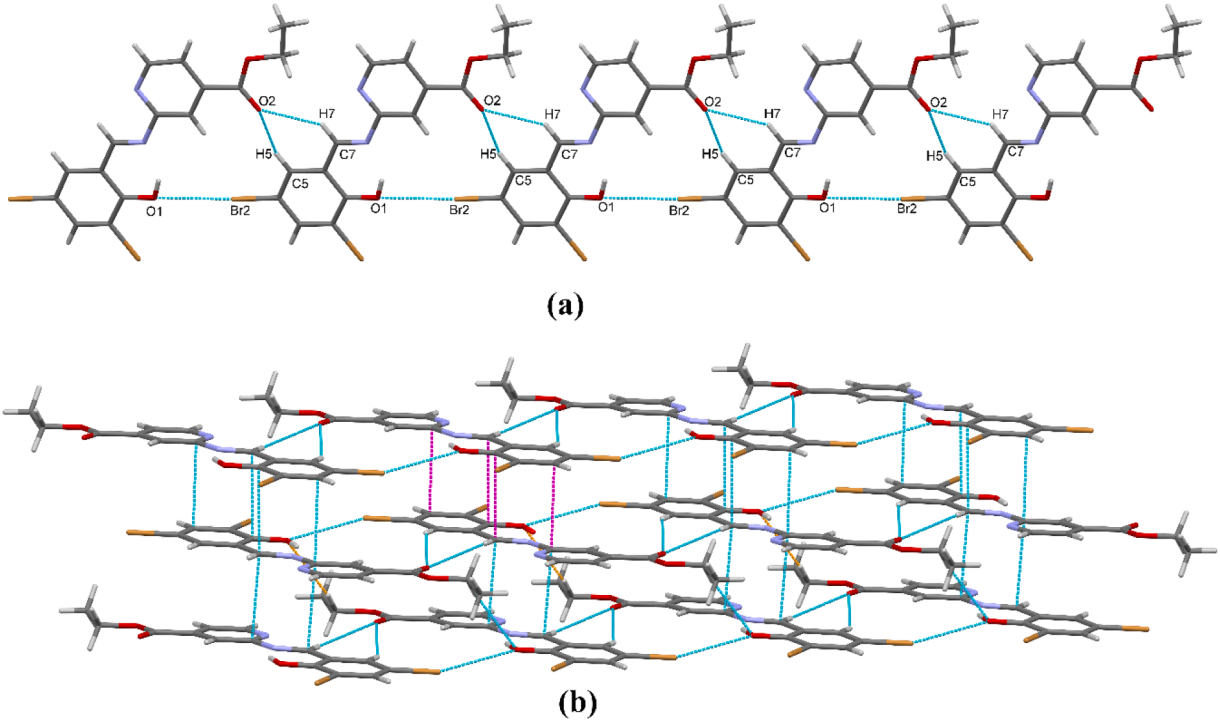

Fig. 3. (a) An infinite 1-D chain formed by C—H···O and O···Br contacts (b) 2-D packing construction by parallel displaced π···π stacking interactions in di-bromo substituted Schiff base compound.

(C7···C8 and C8···C7) and centroid–centroid (Cg1···Cg2) interactions between the aromatic rings of inversion dimers, effectively linking adjacent 2D sheets. Additionally, parallel displaced interactions (C1···C7 and C3···C8) further enhance the supramolecular architecture of the crystal.

3.2. Non-covalent interactions

3.2.1. Hirshfeld surface analysis

Fig. 4 illustrates the Hirshfeld surface (HS) of the mono- and di-bromo substituted Schiff base compounds, mapped over d_{norm}, shape index, and curvedness, effectively highlighting the key regions involved in intermolecular interactions.

For compound 1, the d_{norm}-mapped surface reveals a bright red region near the carbonyl group, corresponding to a prominent C–H···O hydrogen bond, confirming its contribution to crystal stabilization. While compound 2 displays two intense red spots near Br2 and the C5–H5 group, as shown in Fig. 4(a). These regions reflect significant Br2···O1 halogen bonding and C5–H5···O2 hydrogen bonding, respectively. Additional red regions near the –OH group and carbonyl oxygen are attributed to C14–H14B···O1 and C10–H10···Br1 interactions, which play key roles in constructing the 3D packing motif. Smaller, less intense

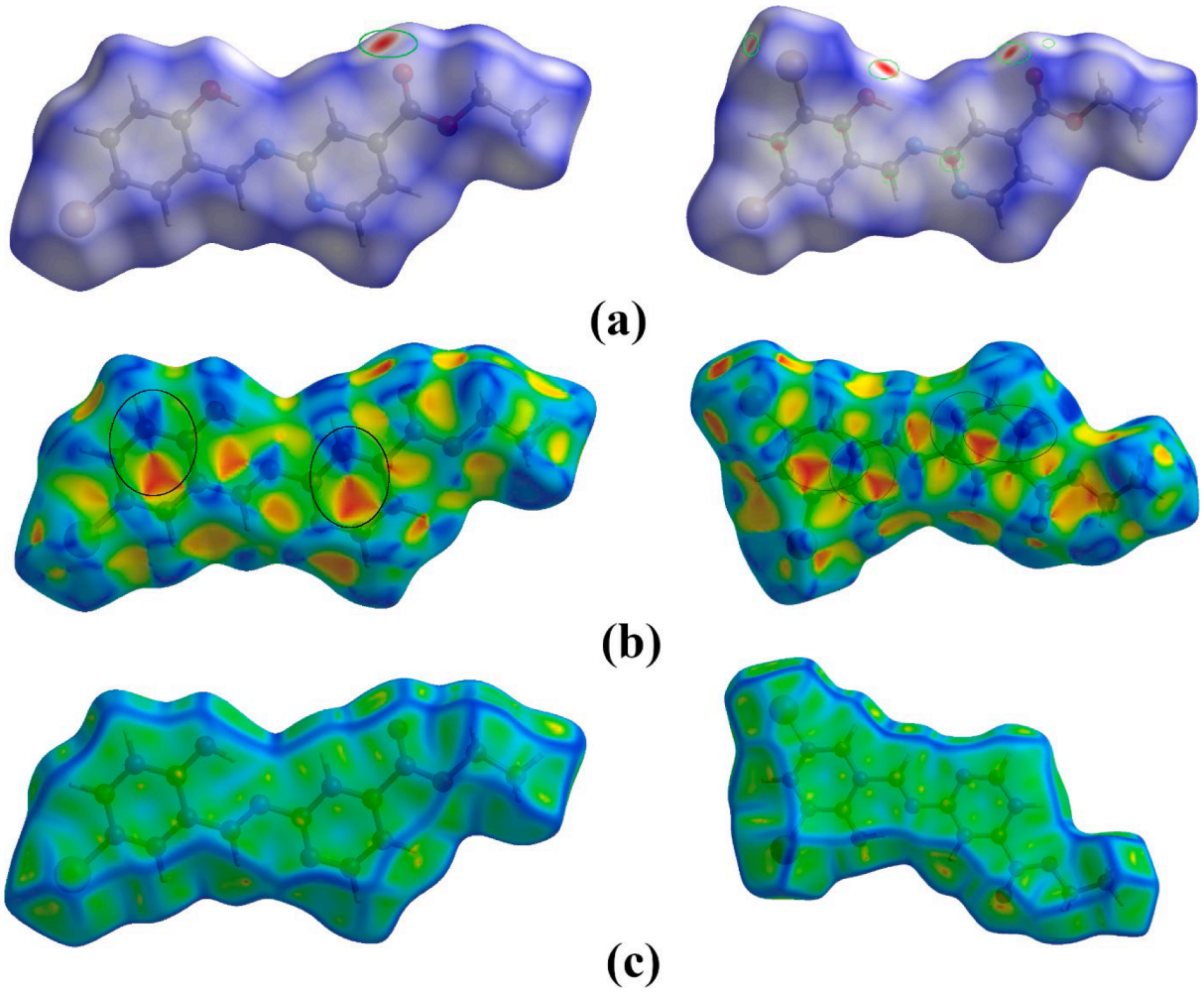

Fig. 4. Normalized (a) d_{norm}, (b) shape index and (c) curvedness property mapped surface with highlighting interacting regions.

red spots are observed near C1 and C3 of the phenyl ring, and C8 and C7 of the pyridine and azomethine moieties, respectively—these correspond to π···π stacking interactions between aromatic systems.

The presence of these π-stacking interactions is further substantiated by the shape index map in Fig. 4(b), where characteristic "bow-tie" patterns (alternating red and blue regions) at the centroids of the phenyl and pyridine rings signify face-to-face stacking. Complementarily, the curvedness map in Fig. 4(c) displays extended flat green regions over the azomethine bridge and both aromatic rings, indicating planar surfaces conducive to stacking. These analyses collectively affirm the importance of hydrogen bonding, halogen bonding, and π interactions in stabilizing the crystal lattice of mono and di-bromo-substituted Schiff base derivatives.

3.2.2. *Fingerprint and enrichment ratio analyses*

The supramolecular architecture of mono-bromo substituted Schiff base compound (compound 1) was elucidated through Hirshfeld surface fingerprint analysis (Fig. 5) complemented by enrichment ratio calculations, offering quantitative insights into the nature of intermolecular contacts within the crystal. Among the observed interactions, H···H contacts constituted the largest proportion (38.1 %), reflecting dominant van der Waals forces, although their enrichment ratio (ER = 1.05) suggests a slight preference consistent with their surface abundance. Significant contributions from H···Br (13.4 %) and H···O (14.6 %) interactions were observed, with respective enrichment ratios of 1.33 and 1.21, indicating a thermodynamic preference for both halogen bonding and C–H···O hydrogen bonding. Particularly notable is the high enrichment of C···C contacts (ER = 3.30), which strongly supports the presence of π…π stacking interactions that enhance crystal packing efficiency and structural stability. In contrast, contacts involving Br···C, Br···N, and Br···Br were significantly underrepresented (ER ≈ 0), suggesting these interactions are sterically or electrostatically disfavored (Table 3).

FP analysis of di-bromo substituted Schiff base compound (compound 2) gives the quantitative contribution of each contact in which H···H (26.3 %) and H···Br (25.1 %) contacts contribute nearly 51 % of the overall contacts of HS. The FP plot mapped over d_i and d_e bins is represented in Fig. 6. The scattered points in the middle of FP at $d_e \approx d_i \approx$ 2.2 Å represent H···H contacts, which are close to the sum of vdW radii. Two wings with the sharp spike at the edges at $d_e + d_i \approx 2.9$ Å signify the halogen-based hydrogen interactions (H···Br contacts). The strong C—H···O hydrogen bonds (14.1 %) are majorly involved in the crystal packing, which is shown by the two symmetrical sharp spikes at $d_e + d_i \approx 2.4$ Å (Table 3). The horn-shaped scattered plot with peaks at $d_e + d_i \approx$ 3.1 Å indicates the C···H contacts. Further, C···C contacts (8.6 %) are important interactions which lead to enriched stacking interactions in molecular packing, evident by the characteristic pale blue to the green area in the centre at $d_e + d_i = 3.6$ Å.

The Hirshfeld surface analysis of compound 2, complemented by enrichment ratio calculations, provides detailed insights into the intermolecular interactions governing its crystal packing. The most dominant interaction was identified as H···Br, accounting for 25.1 % of the total contacts and exhibiting a significantly high enrichment ratio (ER = 1.5), underscoring the preferential formation of halogen bonds within the

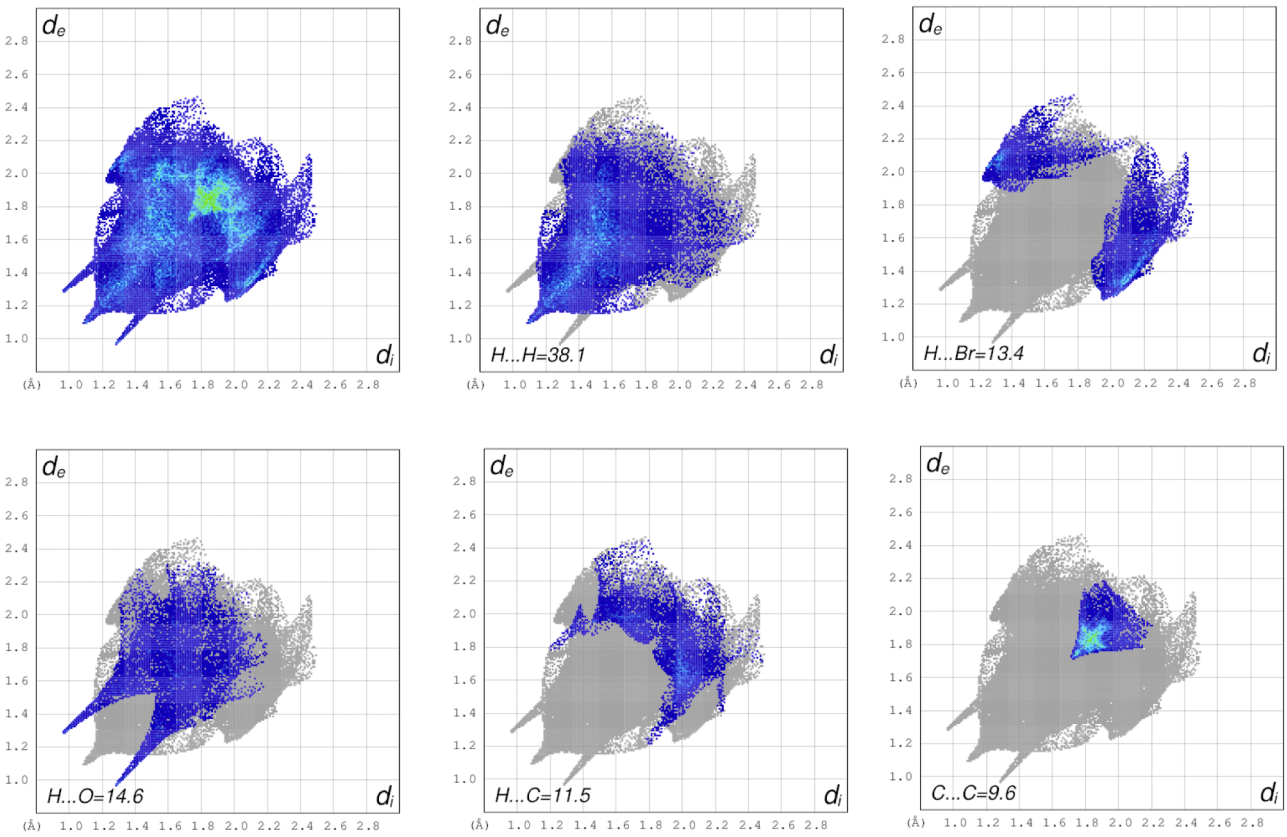

Fig. 5. Fingerprint plots of major inter contacts of the mono-bromo-substituted compound.

Table 3
The percentage contribution of individual interaction and enrichment ratio of mono-bromo-substituted compound.

Compound 1	H	C	O	N	Br
H	38.1			Actual contacts	
C	11.5	9.6			
O	14.6	1	0.4		
N	5	1.8	0.9	0.5	
Br	13.4	0.6	2.7	0	0
Sx	60.35	17.05	10	4.35	8.35
H	36.42			Random contacts	
C	20.58	2.91			
O	12.07	3.41	1.00		
N	5.25	1.48	0.87	0.19	
Br	10.08	2.85	1.67	0.73	0.70
E_{XX}				Enrichment ratio	
H	**1.05**				
C	0.56	**3.30**			
O	**1.21**	0.29	0.40		
N	0.95	**1.21**	-	-	
Br	**1.33**	0.00	-	0.00	-

lattice. Additionally, strong π–π stacking interactions were evidenced by the notable C···C contact enrichment (ER = 3.0), characteristic of planar or aromatic moieties that contribute to extended supramolecular stabilization. Directional hydrogen bonding interactions, particularly H···O (ER = 1.4), further reinforced the structural integrity through moderate electrostatic attraction. In contrast, contacts such as Br···Br, Br···N, and O···O exhibited markedly low enrichment values (ER < 0.2), suggesting their thermodynamic unfavorability and steric incompatibility in the crystal matrix. The relatively depleted H···H interactions (ER = 0.9), compared to compound 1, indicate a packing environment that favors specific polar and π-driven interactions over non-directional dispersive forces (Table 4).

3.3. Quantum theory of atoms in molecule (QTAIM) analysis

The quantum topological approach is used to compute topological parameters at the bond critical points (BCPs) for intramolecular interactions of the molecule and intermolecular contacts in dimeric pairs to evaluate the nature and strength of these interactions. As we observed in the crystal structure analysis, the molecular fragments interact through noncovalent interactions like hydrogen bonding, van der Waals forces, or π-π stacking interactions to stabilize the crystal packing.

The NCI isosurface of the mono- and di-bromo substituted Schiff base derivative is shown in Figs. 7 and 8. The blue and green coloured regions observed in the NCI isosurface are evident in the O—H···N, O···Br, C—H···N, C—H···O intracontacts. The observed low-gradient spike in the 2-D scatter plots at negative values (−0.02 to −0.01 a.u.) is indicative of attractive noncovalent interactions. The steric repulsion at the ring centres is denoted by the red-coloured spikes in the region (sign(λ2) ρ(r) ≈ 0.02 a.u.). The Schiff base molecule exhibited strong intramolecular interactions, as evidenced by the blue-coloured isosurface in Fig. 8, indicative of strong hydrogen bonding.

Furthermore, the molecular interactions of mono- and di-bromo-substituted Schiff base derivatives are also characterized using bond critical points. The π···π interactions between aromatic rings (C3···C11 and C1···C8) in compound 1 are evident from the green-colored region in the isosurface, as shown in Fig. S10. In compound 2, the BCPs correspond to the intermolecular O1···Br2, C7-H7···O1, C5-H5···O1 interaction and π···π (C3···C8, C7···C1 and C7···C8) are identified and characterized (Fig. S4 and Table 5). Using ρ(r) at this BCP, the H-bond binding energy in kcal mol^{-1} could be evaluated as BE = −223.08*ρ(r)+ 0.7423 [42]. It is shown that the intermolecular O···Br contacts are significant contact with an energy of −2.8850 kcal/mol. The strength of C7-H7···O1 and C5-H5···O1, hydrogen bonding interactions, are lesser compared to O···Br with E_{int} of −1.7731 and −2.1337 kcal/mol. Finally, weak π···π stacking interactions, which are majorly involved in the

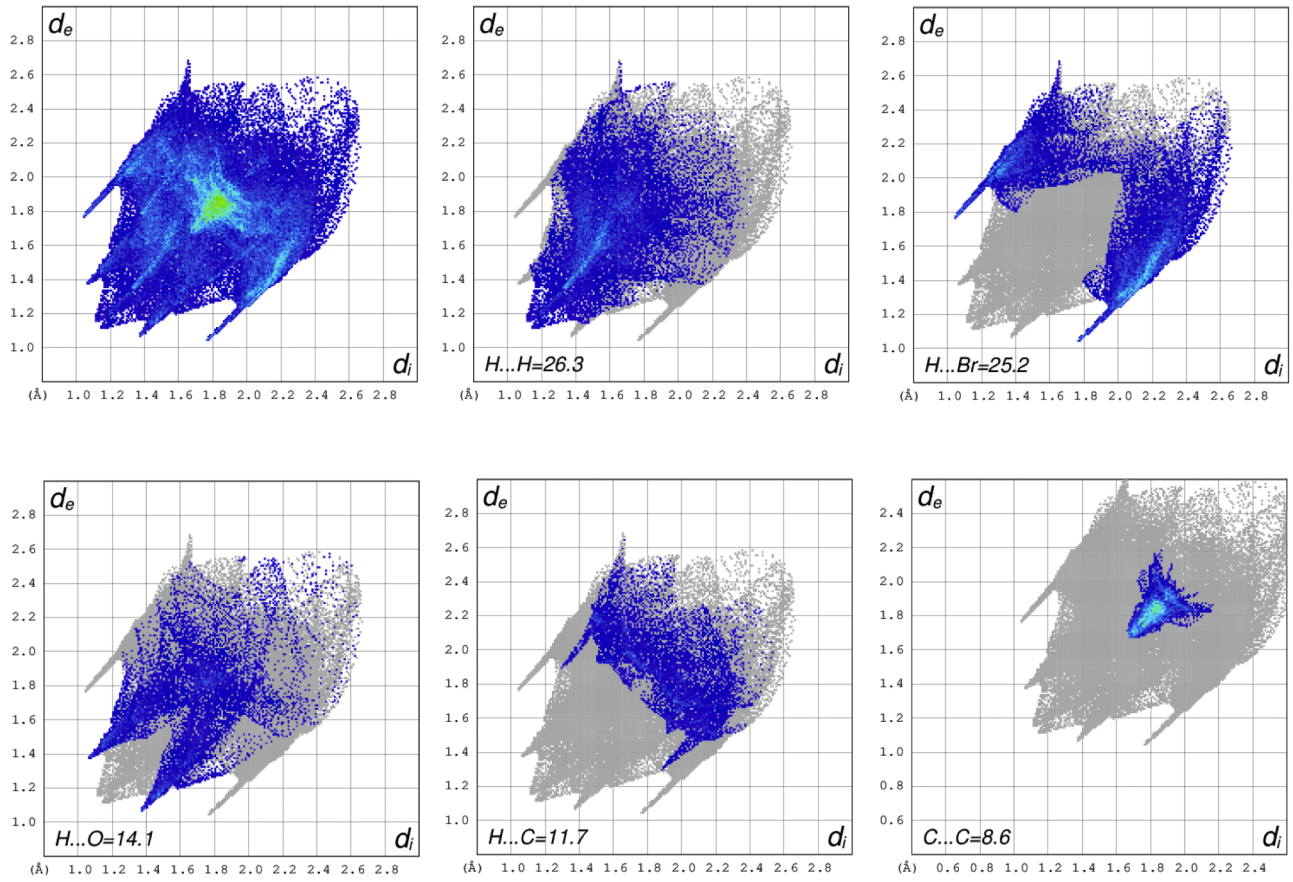

Fig. 6. Fingerprint plots of major inter contacts of the di-bromo-substituted compound.

Table 4
The percentage contribution of individual interaction and enrichment ratio of di-bromo-substituted compound.

Compound 2	H	C	O	N	Br
H	26.3			Actual contacts	
C	11.7	8.6			
O	14.0	0.9	0.1		
N	3.6	2.9	0.1	0.5	
Br	25.1	1.4	3.7	0.6	0.5
Sx	53.5	17.1	9.5	4.1	15.9
H	28.6			Random contacts	
C	18.2	2.9			
O	10.1	3.2	0.9		
N	4.4	1.4	0.8	0.2	
Br	17.0	5.4	3.0	1.3	2.5
E_{XX}				Enrichment ratio	
H	0.9				
C	0.6	**3.0**			
O	**1.4**	0.3	0.1		
N	0.8	**2.1**	0.1	0.0	
Br	**1.5**	0.3	**1.2**	0.0	0.2

stabilization of crystal packing of the compound, are shown lesser energy, which is given in Table 5 and depicted in Fig. S11.

3.4. DFT studies

Molecular geometry optimization by an electronic structure method was performed using initial atomic coordinates of the crystal structure. The best fit between the structural conformation of the optimized and crystal structure was evident by the overlay with the rmsd value of 0.149 and 0.141 Å (Fig. S12 and S13). A comparison of the bond lengths, bond angles and torsional angles also shows a good correlation with the experimental data (Table S1-S6).

Understanding the frontier molecular orbitals (FMOs) of molecules is fundamental to evaluating their electronic structure, reactivity, and potential stability in various chemical and biological environments. The HOMO–LUMO energy gap (Eg) serves as a critical indicator of these properties.

The mono-bromo-substituted compound exhibited HOMO and LUMO energies of −6.3267 eV and −2.7451 eV, respectively, resulting in an energy gap of 3.5816 eV (Fig. 9a). The associated global reactivity descriptors highlight its electronic characteristics: an ionization energy (I) of 6.3267 eV, electron affinity (A) of 2.7451 eV, and an electronegativity (χ) of 4.5359 eV. The calculated chemical potential (μ) was −4.5359 eV, indicating the molecule's electron-donating tendency. Its global hardness (η = 1.7908 eV) and softness ($s = 0.5584\ eV^{-1}$) suggest moderate resistance to electronic deformation, while an electrophilicity index (ω) of 5.7444 eV reflects a reasonable propensity to accept electrons in electrophilic environments. For the di-bromo-substituted Schiff base derivative, the HOMO energy was calculated as −6.4600 eV and the LUMO as −2.8912 eV, yielding an Eg of 3.5688 eV comparable to compound 1 (Fig. 10a). This relatively wide energy gap implies low chemical reactivity and high electronic stability, attributes that may enhance the molecule's resilience in biological environments and reduce the likelihood of spontaneous redox reactions. Collectively, these parameters evident that both molecules show moderate reactivity, good thermodynamic stability, and potential applicability in chemical biology or materials science, particularly where a controlled electronic response is desired (Table 6).

The MEP map is a widely used quantum chemical descriptor for visualizing the spatial distribution of electrostatic potential across a molecule's surface. This property is critical for identifying potential sites of intermolecular interactions, especially electrophilic and nucleophilic

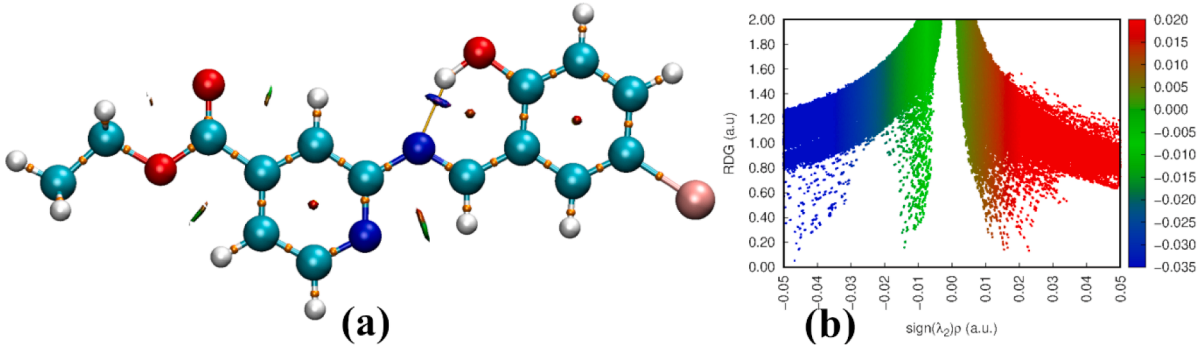

Fig. 7. The 3D and 2D plots of AIM associated with NCI mono-bromo-substituted compound.

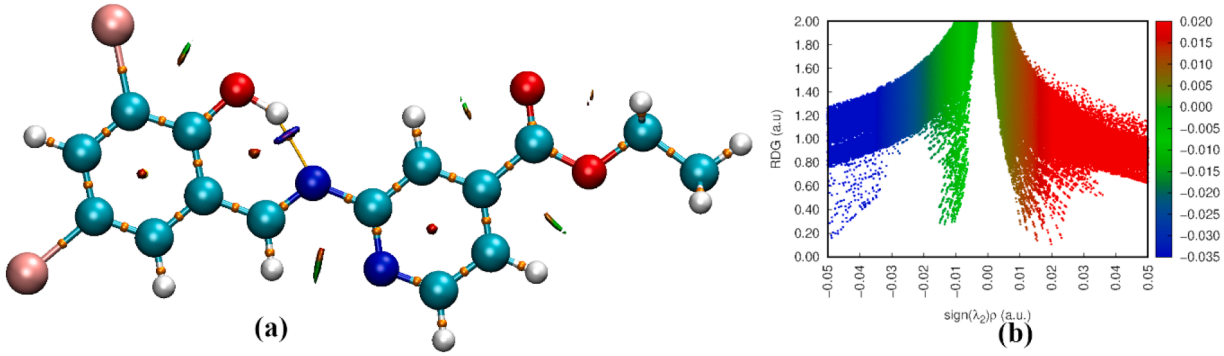

Fig. 8. The 3D and 2D plots of AIM associated with NCI di-bromo-substituted compound.

Table 5
Topological parameters [ρ(r): electron density, $\nabla^2\rho(r)$: Laplacian of electron density; V(r): potential energy density, G(r): kinetic energy density; H(r): total energy density; E_{int}: kcal mol^{-1}] for intra and intermolecular interactions of the di-bromo-substituted compound.

Bonding interaction	ρ (r)	$\nabla^2\rho(r)$	G(r)	V(r)	H(r)	E_{int} (kcal/mol)
O1-H1···N1*	0.0495	0.1083	0.0362	−0.0454	−0.0091	−14.876
O1···Br2#	0.0096	0.0325	0.0071	−0.0060	0.0010	−2.8850
C7-H7···O2#	0.0059	0.0193	0.0040	−0.0033	0.0007	−1.7731
C5-H5···O2#	0.0071	0.0241	0.0049	−0.0039	0.0010	−2.1337
C3···C8#	0.0041	0.0151	0.0028	−0.0018	0.0009	−1.2321
C7···C1#	0.0038	0.0135	0.0024	−0.0015	0.0008	−1.1420
C7···C8#	0.0034	0.0131	0.0023	−0.0014	0.0009	−1.0217

* : intra,.
# : inter.

attack, hydrogen bonding, and metal coordination. The color-coded MEP surfaces allow direct interpretation of reactive regions: red indicates electron-rich (nucleophilic) sites, blue indicates electron-deficient (electrophilic) sites, and green/yellow denote neutral potential zones.

For the di-bromo-substituted Schiff base derivative (Fig. 10b), the MEP surface reveals highly electronegative regions around the hydroxyl (–OH) and carbonyl (*C═O*) moieties, with potential values of −0.0422 a.u. and −0.0410 a.u., respectively (Fig. 10(b)). These areas serve as favorable sites for electrophilic interaction, such as metal ion coordination or hydrogen bonding. Conversely, positive potential regions are concentrated around the phenyl –CH groups (+0.0177 to +0.0268 a.u.), the pyridine ring hydrogens (+0.0260 to +0.0273 a.u.), and the ester methyl group (+0.0266 a.u.), which may act as electron donors in nucleophilic interactions. Interestingly, the substituted bromine atoms, Br1 (−0.0170 a.u., +0.0090 a.u.) and Br2 (−0.0139 a.u., +0.01142 a.u.), exhibit ambivalent behavior with both donating and accepting potential, indicating their possible role in halogen bonding or dual-mode interactions.

In comparison, the mono-bromo-substituted Schiff base derivative (Fig. 9b) shows similar patterns of electrostatic distribution but with distinct localization of charge. The most nucleophilic regions (deep red zones) are centered around carbonyl and phenolic oxygen atoms, which are key targets for electrophilic reagents or coordination to metal centers. The electrophilic (blue) zones are distributed near hydrogens bonded to nitrogen, suggesting their involvement in intramolecular hydrogen bonding or external nucleophilic attack. The central aromatic and heterocyclic system maintains a relatively neutral potential, suggesting a delocalized π-electron environment that contributes to the compound's electronic stability while limiting its polarity-driven reactivity. The MEP analyses for both compounds highlight oxygen-containing functional groups as key electrophilic sites, and electron-deficient hydrogen atoms or alkyl substituents as the primary nucleophilic centers.

A comprehensive evaluation of the second-order perturbation analysis reveals three major categories of stabilizing interactions within the mono-bromo-substituted Schiff base structure. Most prominently, a remarkably high stabilization energy ($E^{(2)}$ = 454.29 kcal/mol) was observed for the LP(O3) → LP*(H4) interaction, suggesting strong intramolecular hydrogen bond, a possible charge-assisted effect. Additional lone pair (LP) interactions involving oxygen and nitrogen atoms with adjacent antibonding orbitals displayed $E^{(2)}$ values ranging from 30 to 50 kcal/mol, indicating significant lone-pair delocalization that contributes to intramolecular stabilization (Table 7). Furthermore, delocalizations such as BD*(C18–C19) → BD*(C16–C24), characteristic of π→π* interactions, were associated with high stabilization energies (150–237 kcal/mol), consistent with extended conjugation and aromatic character across the molecular framework. Lastly, hyperconjugative σ–σ* interactions were evident in donor–acceptor transitions between σ bonds, such as C–H and N–C, showing moderate

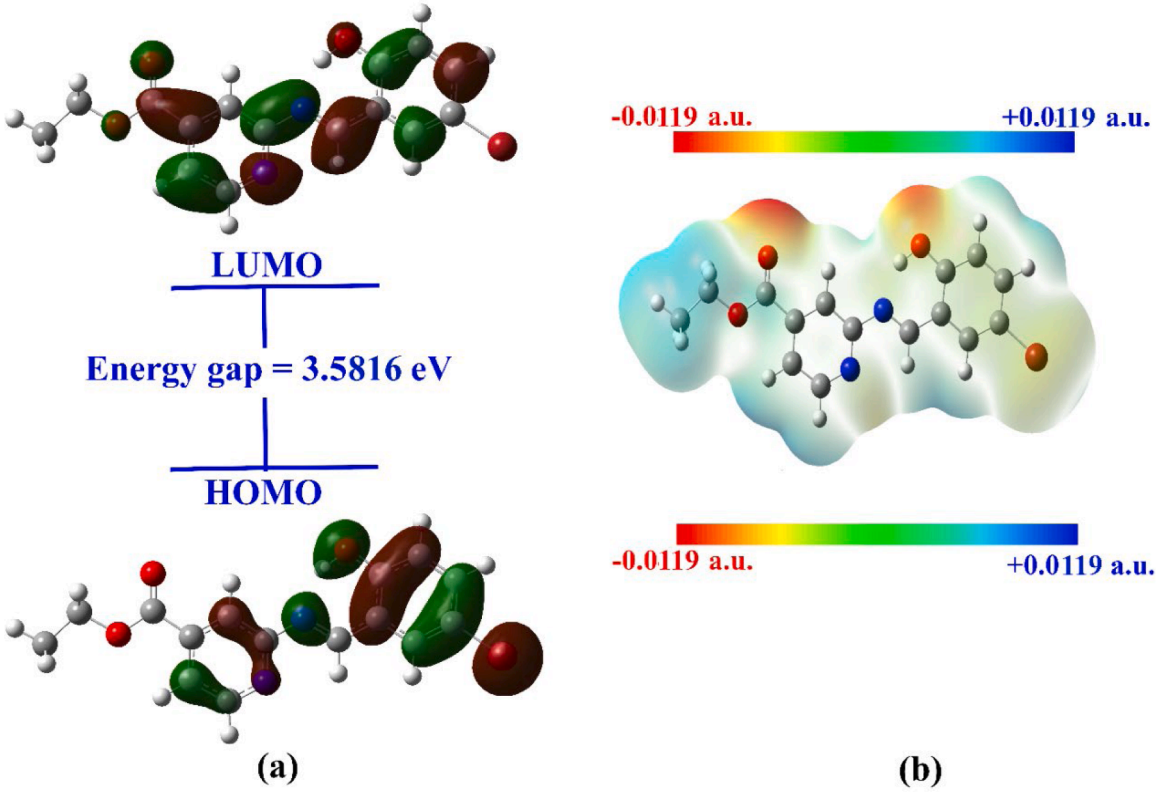

Fig. 9. Frontier molecular orbitals along with energy gap and MEP of the mono-bromo substituted Schiff base compound.

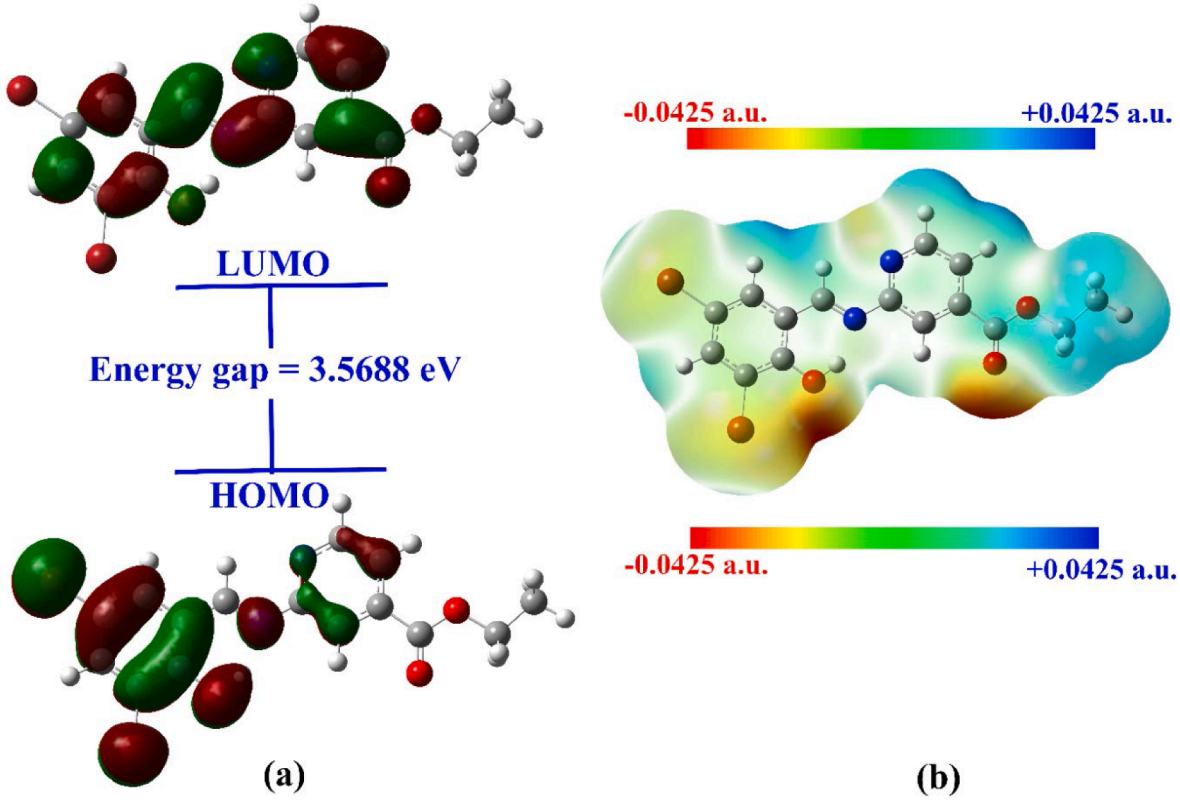

Fig. 10. Frontier molecular orbitals along with energy gap and MEP of the di-bromo substituted Schiff base compound.

Table 6
The global and local reactive parameters of the compounds based on HOMO and LUMO values.

Parameter	Compound 1	Compound 2
Ehomo (Hartree)	−0.2325	−0.2374
Elumo (Hartree)	−0.1008	−0.1062
Ehomo (eV)	−6.3267	−6.4600
Elumo (eV)	−2.7451	−2.8912
Energy gap (Eg) (eV)	3.5816	3.5688
Ionization energy (I) (eV)	6.3267	6.4600
Electron Affinity (A) (eV)	2.7451	2.8912
Electronegativity (χ) (eV)	4.5359	4.6756
Chemical Potential (μ) (eV)	−4.5359	−4.6756
Global hardness (η) (eV)	1.7908	1.7844
Global softness (s) eV^{-1}	0.5584	0.5604
Electrophilicity index (ω) (eV)	5.7444	6.1257

$E^{(2)}$ values (29–75 kcal/mol), which reflect their role in stabilizing the electron density in aliphatic regions and fine-tuning the overall molecular conformation.

While in di-bromo-substituted Schiff base derivative, the natural bond orbital analysis results (Table 7) show that σ and π occupancies are nearly 1.980 and 1.620e, respectively, for –CH and C—C bonds. The analysis of the second-order perturbation theory of the Fock matrix yielded stabilization energies ($E^{(2)}$), which provide insights into the strength of various interactions in the molecule, such as bond strengths and charge transfer effects. A higher $E^{(2)}$ value is observed between the electron donor and acceptor (O1-H1), exhibiting the highest stabilization energy of 447.57 kcal/mol. The other donor-acceptor interactions, along with their $E^{(2)}$ values, are presented in Table 8.

3.5. Molecular docking studies

Molecular docking analyses targeting the bacterial tyrosyl-tRNA synthetase (TyrRS) from *Staphylococcus aureus*, both mono and di-bromo-substituted Schiff base derivatives (Figs. 11 and 12) exhibited substantial binding affinities, underscoring their potential as lead compounds for antibacterial development. Di-bromo-substituted Schiff base derivative demonstrated a slightly stronger binding affinity of −7.3 kcal/mol, engaging the enzyme's N-terminal α/β domain primarily through a hydroxyl-mediated hydrogen bond with GLY193 at a distance of 3.05 Å. Additional stabilizing interactions included a carbon–hydrogen bond between the centroid of the ligand ring and GLY193 (3.94 Å), as well as contact between GLN190 and a carbon atom of the ligand (Fig. 12). In contrast, mono-bromo-substituted Schiff base derivative, with a binding affinity of −6.9 kcal/mol, established a more diversified interaction profile. This included multiple hydrogen bonds with GLY193, GLN190, and GLN196, π–anion and π–alkyl interactions involving ASP195, LEU70, TYR36, and PRO53, and carbon–hydrogen bonds with ASP80 and ASP195. π-based interactions, such as π–π stacking and π–cation interactions, are essential noncovalent forces that significantly influence molecular recognition and stability in biological systems. They contribute to the structural integrity of protein–ligand complexes, enhance binding specificity and affinity, and play a key role in drug–receptor interactions. Understanding these interactions aids in

Table 7
Second-order perturbation theory analysis along with their interaction energy of mono-bromo substituted Schiff base compound.

Occupancy	Type	Donor	Occupancy	Type	Acceptor	E(2)	F(i, j)	E(i)
1.56571	LP (3)	O 3		LP*(1)	H 4	454.29	0.59	0.47
0.44493	π*	C 18 - C 19	0.29886	π*	C 16 - C 24	237.06	0.01	0.083
0.35733	π*	C 12 - C 14	0.29886	π*	C 16 - C 24	196.28	0.01	0.08
0.20431	π*	N 6 - C 22	0.44493	π*	C 18 - C 19	174.78	0.01	0.074
0.43708	π*	N 7 - C 13	0.32643	π*	C 9 - C 10	164.96	0.02	0.087
0.43708	π*	N 7 - C 13	0.29475	π*	C 20 - C 33	148.63	0.02	0.079
0.24299	π*	O 5 - C 8	0.32643	π*	C 9 - C 10	132.67	0.01	0.073
1.98188	σ	C 33 - H 34	0.00814	σ*	C 29 - H 32	75.13	5.39	0.569
1.78766	LP(2)	O 2	0.24299	π*	O 5 - C 8	47.36	0.34	0.114
1.80487	LP(2)	O 3	0.44493	π*	C 18 - C 19	38.02	0.32	0.106
1.98188	σ	C 33 - H 34	0.01213	π*	C 24 - H 25	36.61	1.59	0.216
1.84953	LP(2)	O 5	0.0961	σ*	O 2 - C 8	31.95	0.64	0.129
1.98403	σ*	C 20 - C 33	0.00814	σ*	C 29 - H 32	30.38	5.59	0.369
1.98422	σ	N 7 - C 33	0.00814	σ*	C 29 - H 32	29.35	5.71	0.366
1.63128	π	C 9 - C 10	0.43708	π*	N 7 - C 13	26.32	0.27	0.076

Table 8
Second-order perturbation theory analysis along with their interaction energy of di-bromo substituted Schiff base compound.

Occupancy	Type	Donor	Occupancy	Type	Acceptor	$E^{(2)}$	F(i, j)	$E^{(i)}$
1.57175	LP(3)	O1	1.96503	LP*(1)	H1	447.57	0.59	0.466
1.78713	LP(2)	O3	0.24275	π*	O2-C13	47.43	0.34	0.114
1.98792	σ	C15-H15C	0.00813	σ*	C15-H15A	44.58	5.07	0.425
1.86812	LP(1)	N1	1.96503	LP*(1)	H1	41.83	0.5	0.142
1.7962	LP(2)	O1	0.44937	π*	C6-C1	39.28	0.32	0.107
1.98792	σ	C15-H15C	0.0041	σ*	C15-H15C	34.13	3.57	0.312
1.84934	LP(2)	O2	0.09596	σ*	O3-C13	31.91	0.64	0.129
1.62811	π	C12-C11	0.43825	π*	N2-C8	26.51	0.26	0.076
1.98792	σ	C15-H15C	0.03333	σ*	C7-H7	26.27	1.39	0.171
1.69016	Π	N2-C8	0.29393	π*	C10-C9	25.53	0.33	0.083
1.56486	Π	C6-C1	0.36598	π*	C4-C5	24.12	0.27	0.074
1.71618	Π	C14-C17	0.3625	π*	C15-C19	22.4	0.29	0.073
1.99087	σ	C24-C31	0.0041	σ*	C31-H33	22.16	3.71	0.256
1.98792	σ	C31-H32	0.00813	σ*	C31-H34	22.01	5.08	0.299
1.56486	Π	C9-C20	0.19966	π*	N7-C12	21.95	0.26	0.072

$E^{(2)}$: Stabilization energy.
F(i, j): Off-diagonal Fock matrix element of i and j.
$E^{(i)}$ represents the energy of the donor orbital (i), while $E^{(j)}$ corresponds to the energy of the acceptor orbital (j) in NBO analysis.

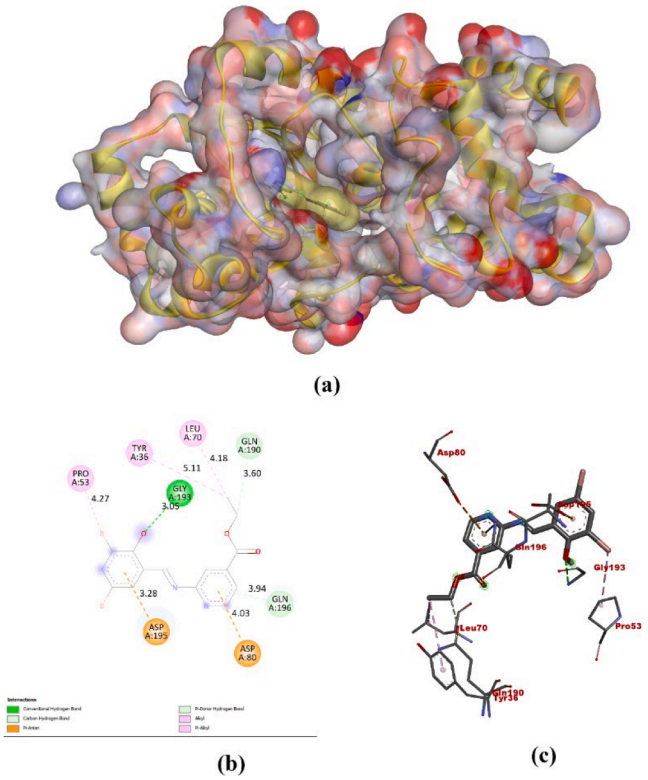

Fig. 11. The molecular docking poses illustrate the diverse interactions between the ligand (compound 1) and the protein.

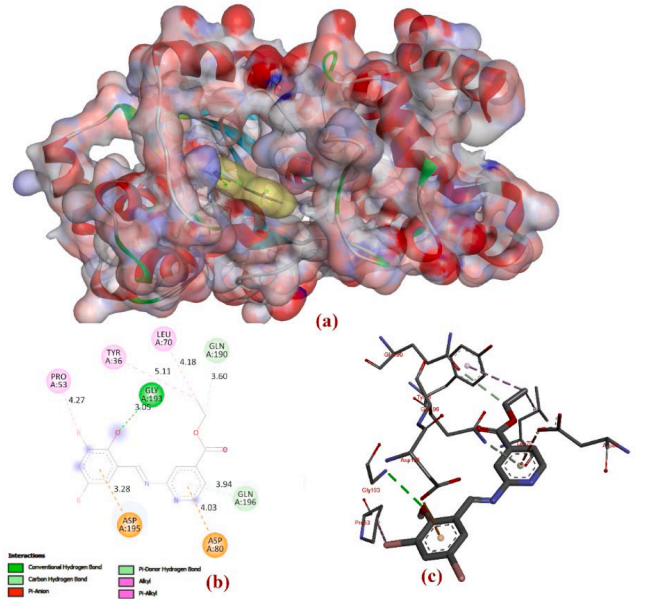

Fig. 12. The molecular docking poses illustrate the diverse interactions between the ligand (compound 2) and the protein.

rational drug design by identifying ligands with improved biological activity and target selectivity. In the present study, despite the marginally weaker binding affinity, the broader and more complex π-based interaction network suggests enhanced conformational stabilization within the active site, thereby highlighting complementary strategies in ligand design for TyrRS inhibition (Fig. 11).

4. Conclusion

In this study, we investigated the influence of mono- and di-bromo substitution at the meta positions of the phenyl ring in Schiff base derivatives. Structural and computational analyses revealed that both compounds maintain planarity, with small dihedral angles supporting robust π···π stacking interactions that stabilize the crystal packing. The di-bromo derivative exhibited additional chalcogen and halogen (Br…O) interactions, further enhancing packing stability. Enrichment ratio analysis confirmed the significance of π···π stacking (enrichment value of 3.0), while QTAIM analysis highlighted distinctive van der Waals interactions between aromatic rings. Overall, meta-bromo substitution had minimal impact on crystal packing but influenced electron density distribution within the phenyl ring. Molecular docking studies demonstrated that π-based interactions between ligand centroid rings and amino acid residues contribute to enhanced conformational stability within the TyrRS active site. These findings provide comprehensive insights into how positional substitution governs molecular packing, noncovalent interactions, and potential biological activity, offering valuable guidance for the rational design of functional crystalline materials and bioactive compounds.

Appendix A. Supplementary data: CCDC 2478800 and 2351,696 contains the supplementary crystallographic data of the Schiff base compound. The data can be obtained free of cost via http://www.ccdc.cam.ac.uk/conts/retrieving.html, or from the Cambridge Crystallographic Data Centre, 12 Union Road, Cambridge CB2 1EZ, UK; fax: (+44) 1223–336–033; or e-mail: deposit@ccdc.cam.ac.uk.

CRediT authorship contribution statement

Udaya Kumar A. H.: Conceptualization, Investigation, Validation, Writing – original draft, Writing – review & editing. **Yuvaraja Dibdalli:** Data curation, Formal analysis, Resources. **Cesar Morales-Verdejo:** Data curation, Formal analysis, Resources, Software, Validation. **Nagesh Khadri M. J.:** Data curation, Formal analysis, Validation. **Mahesha:** Conceptualization, Investigation, Methodology, Supervision, Writing – original draft, Writing – review & editing. **Lokanath N. K.:** Conceptualization, Project administration, Resources, Software, Supervision, Writing – review & editing.

Declaration of competing interest

We declare that we have no conflict of interest in any direction for the manuscript.

Acknowledgements

The authors are thankful to the DST-FIST program (*SR/FST/PSI-119/2019)*, National Single Crystal Diffractometer Facility, DoS in Physics, CPEPA, and DST-PURSE, Vijnana Bhavan, University of Mysore, Mysuru.

Supplementary materials

Supplementary material associated with this article can be found, in the online version, at doi:10.1016/j.molstruc.2025.144582.

Data availability

Data will be made available on request.

References

[1] G.R. Desiraju, Crystal engineering: from molecule to crystal, J. Am. Chem. Soc. 135 (2013) 9952–9967, https://doi.org/10.1021/JA403264C/ASSET/IMAGES/MEDIUM/JA-2013-03264C_0014.GIF.

[2] D. Braga, F. Grepioni, L. Maini, S. d'Agostino, From solid-State structure and dynamics to crystal engineering, Eur. J. Inorg. Chem. 2018 (2018) 3597–3605, https://doi.org/10.1002/EJIC.201800234;CTYPE:STRING:JOURNAL.

[3] A.K. Nangia, G.R. Desiraju, Crystal Engineering: an outlook for the future, Angewandte Chemie - Int. Edition 58 (2019) 4100–4107, https://doi.org/10.1002/ANIE.201811313;PAGE:STRING:ARTICLE/CHAPTER.

[4] H. Ai, Q. Li, Q. Xu, X. Li, D. Li, Q. Wu, Halogen substitution for fine-tuning the energy gap and intermolecular interactions of dinuclear iron(III) half schiff base complexes: experimental and theoretical investigation, J. Mol. Struct. 1348 (2025) 143508, https://doi.org/10.1016/J.MOLSTRUC.2025.143508.

[5] G. Kaştaş, Ç.A. Kaştaş, B.K. Kırca, C.C. Ersanlı, The effect of the change in substituents' positions on the formation of supramolecular networks and the solvent type/substituent dependence of prototropic behavior in three new o-hydroxy Schiff bases, J. Mol. Struct. 1200 (2020) 127109, https://doi.org/10.1016/J.MOLSTRUC.2019.127109.

[6] A. Mukherjee, S. Tothadi, G.R. Desiraju, Halogen bonds in crystal engineering: like hydrogen bonds yet different, Acc. Chem. Res. 47 (2014) 2514–2524, https://doi.org/10.1021/AR5001555/ASSET/IMAGES/MEDIUM/AR-2014-001555_0013.GIF.

[7] K. Molčanov, V. Milašinović, B. Kojić-Prodić, Contribution of different crystal packing forces in π-stacking: from noncovalent to covalent multicentric bonding, Cryst. Growth Des. 19 (2019) 5967–5980, https://doi.org/10.1021/ACS.CGD.9B00540/ASSET/IMAGES/MEDIUM/CG9B00540_0017.GIF.

[8] G.R. Desiraju, Crystal engineering: a holistic view, Angewandte Chemie - Int. Edition 46 (2007) 8342–8356, https://doi.org/10.1002/ANIE.200700534;WGROUP:STRING:PUBLICATION.

[9] X. Jin, S. Li, L. Guo, J. Hua, D.H. Qu, J. Su, Z. Zhang, H. Tian, Interplay of steric effects and aromaticity reversals to expand the structural/electronic responses of dihydrophenazines, J. Am. Chem. Soc. 144 (2022) 4883–4896, https://doi.org/10.1021/JACS.1C12610/SUPPL_FILE/JA1C12610_SI_008.MP4.

[10] H.H. Jensen, M. Bols, Stereoelectronic substituent effects, Acc. Chem. Res. 39 (2006) 259–265, https://doi.org/10.1021/AR050189P;WGROUP:STRING:ACHS.

[11] D. Das, R.K.R. Jetti, R. Boese, G.R. Desiraju, Stereoelectronic effects of substituent groups in the solid state. Crystal chemistry of some cubanecarboxylic and phenylpropiolic acids, Cryst. Growth Des. 3 (2003) 675–681, https://doi.org/10.1021/CG0341252/SUPPL_FILE/CG0341252SI20030710_115942.PDF.

[12] K. Hęclik, B. Dębska, J.C. Dobrowolski, On the non-additivity of the substituent effect in ortho-, meta- and para-homo-disubstituted benzenes, RSC. Adv. 4 (2014) 17337–17346, https://doi.org/10.1039/C4RA02294G.

[13] H. Szatylowicz, A. Jezuita, T.M. Krygowski, On the relations between aromaticity and substituent effect, Struct. Chem. 30 (5) (2019) 1529–1548, https://doi.org/10.1007/S11224-019-01360-7, 201930.

[14] S.E. Wheeler, Understanding substituent effects in noncovalent interactions involving aromatic rings, Acc. Chem. Res. 46 (2013) 1029–1038, https://doi.org/10.1021/AR300109N/ASSET/IMAGES/LARGE/AR-2012-00109N_0010.JPEG.

[15] L.M. Salonen, M. Ellermann, F. Diederich, Aromatic rings in chemical and biological recognition: energetics and structures, Angewandte Chemie - Int. Edition 50 (2011) 4808–4842, https://doi.org/10.1002/ANIE.201007560.

[16] D. Das, R.K.R. Jetti, R. Boese, G.R. Desiraju, Stereoelectronic effects of substituent groups in the solid state. Crystal chemistry of some cubanecarboxylic and phenylpropiolic acids, Cryst. Growth Des. 3 (2003) 675–681, https://doi.org/10.1021/CG0341252.

[17] A.E. Kopotilova, M.I. Valieva, E.A. Kudryashova, E.S. Starnovskaya, T. N. Moshkina, E.V. Nosova, O.S. Taniya, A.A. Kalinichev, A.S. Novikov, D. S. Kopchuk, P.A. Slepukhin, V.N. Charushin, Methyl- and methoxy-substituted 2-(Pyridin-2-yl)-4-(4-aminophenyl)quinazolines: synthesis and photophysical properties, Asian J. Org. Chem. 13 (2024) e202400135, https://doi.org/10.1002/AJOC.202400135;WEBSITE:WEBSITE:ACES;CTYPE:STRING:JOURNAL.

[18] S.R. Shankara, K.M. Eshwarappa, J. A, S. Prabhu, R. Pinto, Enhancing nonlinear optical responses via methoxy positional isomerism in chalcone-based materials, Mater. Chem. Phys. 312 (2024) 128662, https://doi.org/10.1016/J.MATCHEMPHYS.2023.128662.

[19] D. Bhat, L. Spoorthy, R. Sharanya, M. Siddesh, A.HU.K. Mahesha, N.K. Lokanath, Influence of hydroxyl group in stabilizing the Schiff base crystal structure: crystal structure, computational and molecular docking studies, J. Mol. Struct. 1280 (2023) 135054, https://doi.org/10.1016/J.MOLSTRUC.2023.135054.

[20] J.W. Pflugrath, The finer things in X-ray diffraction data collection, Urn:Issn:0907-4449 55 (1999) 1718–1725. https://doi.org/10.1107/S090744499900935X.

[21] G.M. Sheldrick, SHELXT – Integrated space-group and crystal-structure determination, Urn:Issn:2053-2733 71 (2015) 3–8. https://doi.org/10.1107/S2053273314026370.

[22] G.M. Sheldrick, IUCr, crystal structure refinement with SHELXL, Urn:Issn:2053-2296 71 (2015) 3–8. https://doi.org/10.1107/S2053229614024218.

[23] A.L. Spek, IUCr, single-crystal structure validation with the program PLATON, Urn: Issn:0021-8898 36 (2003) 7–13. https://doi.org/10.1107/S0021889802022112.

[24] C.F. MacRae, I. Sovago, S.J. Cottrell, P.T.A. Galek, P. McCabe, E. Pidcock, M. Platings, G.P. Shields, J.S. Stevens, M. Towler, P.A. Wood, Mercury 4.0: from visualization to analysis, design and prediction, Urn:Issn:1600-5767 53 (2020) 226–235. https://doi.org/10.1107/S1600576719014092.

[25] J.J. McKinnon, M.A. Spackman, A.S. Mitchell, Novel tools for visualizing and exploring intermolecular interactions in molecular crystals, Urn:Issn:0108-7681 60 (2004) 627–668. https://doi.org/10.1107/S0108768104020300.

[26] M.A. Spackman, D. Jayatilaka, Hirshfeld surface analysis, CrystEngComm. 11 (2009) 19–32, https://doi.org/10.1039/B818330A.

[27] A.H. Udaya Kumar, K.J.P. Mahesha, K. Kumara, M.K. Hema, N.V. Harohally, N. K. Lokanath, Structural-property relationship in halogen-bonded Schiff base derivative: crystal structure, computational and SARS-CoV-2 docking studies, J. Mol. Struct. (2022) 1265, https://doi.org/10.1016/j.molstruc.2022.133409.

[28] A.H. Udaya Kumar, K. Kumara, N.V. Harohally, K.J. Pampa, N.K. Lokanath, Square planar trans-N2O2 Cu(II) complex: synthesis, crystal structure, Hirshfeld surface, DFT, antimicrobial and docking studies, Chem. Select. 6 (2021) 6240–6255, https://doi.org/10.1002/SLCT.202101149.

[29] A.H. Udaya Kumar, K.J. Pampa, N.V.H. Mahesha, D. Das, B.N. Ghosh, N. K. Lokanath, Structural and computational studies of Schiff base ligand and its metal complexes: synthesis, solvent effects by post-synthetic modification, computational and selective hazardous sulfide anion detection, Polyhedron. 243 (2023) 116521, https://doi.org/10.1016/J.POLY.2023.116521.

[30] A.H. Udaya Kumar, K.J. Pampa, N.V. Harohally, D. Das, B.N. Ghosh, N. K. Lokanath, Structural studies of Schiff base ligand and its copper complexes: solvents effect in 1-D polymeric and monomeric copper (II) complexes, computational and sensing studies, Mater. Chem. Phys. 306 (2023) 128031, https://doi.org/10.1016/J.MATCHEMPHYS.2023.128031.

[31] A.H.U.K. Mahesha, K.G. Vindya, K.J. Pampa, K.S. Rangappa, N.K. Lokanath, Structure-property relationship in thioxotriaza-spiro derivative: crystal structure and molecular docking analysis against SARS-CoV-2 main protease, J. Mol. Struct. 1250 (2022) 131746, https://doi.org/10.1016/J.MOLSTRUC.2021.131746.

[32] T.N. Bharath, A.H. Udaya Kumar, K.J.P. Mahesha, A. Ahmad, M.B. Alshammari, K. Karthik, N.K. Lokanath, Structural and computational exploration of zwitterionic and quinoidal forms in Schiff base compound, J. Mol. Struct. (2025) 1319, https://doi.org/10.1016/J.MOLSTRUC.2024.139289.

[33] C. Jelsch, K. Ejsmont, L. Huder, The enrichment ratio of atomic contacts in crystals, an indicator derived from the Hirshfeld surface analysis, IUCrJ. 1 (2014) 119–128, https://doi.org/10.1107/S2052252514003327/ED5001SUP1.PDF.

[34] J. Jayashankar, M. Hema, N, N'-bis (2-bromobenzylidene)-2, 2'-diaminodiphenyldisulfide (BBDD): Insights of Crystal structure, DFT, QTAIM, PASS, ADMET and Molecular Docking Studies, Elsevier, 2022 n.d. https://www.sciencedirect.com/science/article/pii/S0022286022013138. accessed January 7, 2024

[35] T.L.-S. manual. Version, undefined 2014, Multiwfn, Researchgate.NetT LuSoftware Manual. Version, 2014•researchgate.Net (2017). https://www.researchgate.net/profile/Melek-Hajji/post/Can-NCIplot-be-applied-to-systems-containing-Iodine-atom-If-yes-How/attachment/5cb785583843b01b9b9ac642/AS%3A748765837271043%401555531095713/download/Manual_3.4.pdf (accessed December 15, 2023).

[36] Frisch: Gaussian 16, revision C. 01 - Google Scholar, (n.d.). https://scholar.google.com/scholar?cluster=17984419228219957392&hl=en&as_sdt=2005&sciodt=0,5 (accessed December 15, 2023).

[37] GaussView 6 | Gaussian.com, (n.d.). https://gaussian.com/gaussview6/ (accessed August 25, 2022).

[38] X. Qiu, C.A. Janson, W.W. Smith, S.M. Green, P. McDevitt, K. Johanson, P. Carter, M. Hibbs, C. Lewis, A. Chalker, A. Fosberry, J. Lalonde, J. Berge, P. Brown, C.S. V. Houge-Frydrych, R.L. Jarvest, Crystal structure of Staphylococcus aureus tyrosyl-tRNA synthetase in complex with a class of potent and specific inhibitors, Protein Sci. 10 (2001) 2008–2016, https://doi.org/10.1110/PS.18001;JOURNAL:JOURNAL:1469896X;PAGE:STRING:ARTICLE/CHAPTER.

[39] R. Huey, G. Morris, Using AutoDock 4 and AutoDock vina With AutoDockTools: a tutorial, Researchgate.NetR Huey, GM Morris, S ForliThe Scripps Research Institute Molecular Graphics Laboratory, 2012, 2012•researchgate.Net (n.d.), https://www.researchgate.net/profile/Vasanthan-Vasudevan-2/post/Auto-grid-generation-in-Autodock-tool-for-docking/attachment/59d6223fc49f478072e98d56/AS%3A272113926115328%401441888423193/download/example.zip. accessed December 15, 2023.

[40] E. Di Muzio, D. Toti, F. Polticelli, DockingApp: a user friendly interface for facilitated docking simulations with AutoDock Vina, J. Comput. Aided. Mol. Des. 31 (2017) 213–218, https://doi.org/10.1007/S10822-016-0006-1/FIGURES/4.

[41] D.S. Biovia, Discovery Studio Modeling Environment. Dassault Syst. Release, 4, Scientific Research Publishing, San Diego, 2015. - References -n.d. https://www.scirp.org/(S(351jmbntv-nsjt1aadkposzje))/reference/referencespapers.aspx?referenceid=2450411. accessed August 25, 2022

[42] S. Emamian, T. Lu, Exploring nature and predicting strength of hydrogen bonds: a correlation analysis between atoms-in-molecules descriptors, binding energies, and energy, Wiley Online LibraryS Emamian, T Lu, H Kruse, H Emamian J. Computat. Chem. 40 (2019) 2868–2881, https://doi.org/10.1002/jcc.26068. Wiley Online Library2019.